

Experimental Realization of Optimized Ternary Mirror Coatings

V. Pierro,^{1,2} M. Granata,³ C. Michel,³ L. Pinard,³ B. Sassolas,³ D. Forest,³ N. Demos,⁴ S. Gras,⁴ M. Evans,⁴ I. M. Pinto,² G. Avallone,⁵ V. Granata,^{6,2}

¹*Dipartimento di Ingegneria (DING), Università del Sannio,
Piazza Roma, 28, 82100 Benevento BN, Italy*

²*INFN Sezione di Napoli Gruppo Collegato di Salerno,
Complesso Universitario di Monte S. Angelo, 80126 Napoli, Italy*

³*Laboratoire des Matériaux Avancés - IP2I, CNRS,
Université Claude Bernard Lyon 1, F-69100 Villeurbanne, France*

⁴*Massachusetts Institute of Technology, 185 Albany Street
NW22-295, Cambridge, Massachusetts 02139, USA*

⁵*Dipartimento di Fisica “E.R. Caianiello”, Università di Salerno,
Via Giovanni Paolo II, 132, 84084 Fisciano SA, Italy and*

⁶*Dipartimento di Ingegneria Industriale,
Elettronica e Meccanica DIEM, Università di Roma Tre,
Via Vito Volterra, 62, 00146 Roma RM, Italy*

We report on the first experimental realization of multi-material dielectric mirror coatings designed through a multi-objective optimization algorithm to simultaneously minimize thermal noise and optical losses. We validate this design strategy by fabricating and characterizing two distinct ternary systems: a SiN_x -based proof-of-concept and a Ti:GeO_2 -based system targeting lower optical losses. The performance of the SiN_x coating shows remarkable agreement with predictions, demonstrating a noise amplitude spectral density reduction of 0.82 with respect to current reference coatings, and validating our design-to-fabrication pipeline. The Ti:GeO_2 -based system achieves the crucial goal of sub-ppm absorption; its measured thermal noise, however, is higher than the theoretically predicted level of 0.71, extrapolated from single-layer material characterization. A dedicated tolerance analysis confirms that this discrepancy is not attributable to random thickness errors, emphasizing that further studies of the manufacturing process are needed to fully exploit this combination of materials. This work establishes a robust methodology for producing complex, high-performance optical coatings tailored for precision experiments.

Introduction— In the last two decades, optics has reached unprecedented levels of precision and stability. In recognition of this, the United Nations declared 2022 the International Year of Glass, following the International Year of Light, which commemorated the 1,000th anniversary of Al-Hasan Ibn Al-Haytham’s *Kitab al-Manazir* (Book of Optics) [1].

For many advanced optical applications, including high-power [2–4] and ultra-stable lasers [5], optical cavities for precision experiments [6]—even in fundamental physics [7, 9, 17]—and photonic devices [10], the reduction of Brownian thermal noise remains a central challenge despite these advances.

A major obstacle in designing coatings for high-sensitivity optical devices is the difficulty of identifying materials that simultaneously

provide low optical absorption, low Brownian noise, and a sufficiently broad range of refractive indices.

A promising approach is the use of multi-material coatings, which allow thin low-noise but absorptive layers to be buried under noisier yet low-absorption layers [11–13]. Theoretical formulations of this design problem [1, 2], as well as initial demonstrations of feasibility [16], have been reported. Multi-material coatings have been proposed for gravitational-wave interferometers [17], and some preliminary experimental realizations have been achieved as proof-of-concept [18, 19].

In this work, we take a decisive step beyond previous empirical demonstrations: for the first time, we realize two distinct multi-material coatings, both designed through a fully predic-

tive optimization framework. This achievement demonstrates the feasibility of producing advanced ternary coatings by means of an innovative design-to-fabrication pipeline, establishing a new paradigm for the development of high-performance optical coatings.

Design Strategy – To overcome the performance limits of traditional binary stacks, we developed a design framework for multi-material coatings based on a Double-Stack of Doublets (DSD) architecture (see *supplementary material* [20] for details). This design consists of two sub-stacks: a bottom stack near the substrate, made of materials with high refractive index contrast (like $\text{SiN}_x/\text{SiO}_2$ or $\text{Ti:GeO}_2/\text{SiO}_2$) to achieve high reflectivity with fewer layers, and a top stack, made of materials with low optical absorption ($\text{Ta}_2\text{O}_5\text{-TiO}_2/\text{SiO}_2$), to shield the more absorptive layers from the incident laser field. The layer thicknesses are not quarter-wave but are determined by a multi-objective evolutionary algorithm [21] that seeks Pareto-optimal (best-tradeoff) solutions for thermal noise, absorption, and transmittance [16].

Our methodology avoids subjective weighting of the objectives and employs a deterministic, two-stage selection process, as detailed in the supplementary material [20], which leads to the identification of a single optimal design.

To compute the coating properties, our algorithm used a transmission matrix method for the optics [22] and a thermal noise model by Braginsky et al. [23]. In this model, the noise power spectral density S_{CB} is a linear combination of the contributions from each layer, weighted by its thickness d_i and its coefficient η_i :

$$S_{CB}(f) = \frac{2k_B T}{\pi^2 w^2 f} \sum_{i=1}^N \eta_i d_i, \quad (1)$$

where

$$\eta_i = \varphi_i \left[\frac{(1 + \sigma_i)(1 - 2\sigma_i)}{Y_i(1 - \sigma_i)} + \frac{Y_i(1 + \sigma)^2(1 - 2\sigma)^2}{Y^2(1 - \sigma_i^2)} \right]. \quad (2)$$

In Eq. (2), k_B is the Boltzmann constant, T is the mirror temperature, w is the beam

radius, f is the frequency, Y and σ are the Young modulus and Poisson coefficient of the substrate, respectively, and d_i , Y_i , σ_i and φ_i are the thickness, Young modulus, Poisson coefficient and the elastic loss angle of the i -th layer, respectively. The loss angle φ_i quantifies the layer elastic energy dissipation and determines its noise amplitude [24]. Knowledge of the η_i coefficients is thus crucial for making reliable noise predictions. A detailed discussion of the noise model and its limitations is provided in the supplementary material [20].

In this work, we used silicon-rich silicon nitride (SiN_x) and Ti-doped germania (i.e. Ti:GeO_2), as layers of high refractive index, lower noise and higher absorption [17]. The other materials used were Ti-doped tantalum (i.e. $\text{Ti:Ta}_2\text{O}_5$) as high-index layers of higher noise and lower-absorption, and silica (SiO_2) as low-index layers of low noise and absorption, as in current mirror coatings of interferometric gravitational wave detectors [18].

The use of the DSD structure is certainly motivated by its simplicity (theoretical and experimental), but also by certain incompatibilities between the different synthesis conditions of the materials. In particular, a limitation is posed by the onset of crystallization in the $\text{Ti:Ta}_2\text{O}_5$ layers upon thermal treatment (*annealing*), which is standard practice. While the SiN_x and SiO_2 layers might be annealed up to 1000 °C without crystallization [26, 27], the amorphous to poly-crystalline phase transition of the tantalum layers takes place between 650 and 700 °C. To take advantage of the low loss angle of high-temperature annealed SiN_x and SiO_2 , we split our design into two distinct doublet-based binary stacks.

In line with the stringent requirements for mirror coatings in gravitational-wave interferometers, which often include constraints at auxiliary wavelengths (e.g., 532 nm for thermal control systems), our design prioritizes the primary 1064 nm detection band.

We focus on a *single-band* optimization because a *dual-band* approach, which our code can readily handle, would compromise performance in the detection band, our primary goal

being to establish the ultimate performance limit, in terms of thermal noise, at the operating wavelength (see rationale in [20]). The main constraint is therefore a maximum transmittance (τ_c) of 5.6 ppm at a 1064 nm wavelength. The significant difference in the extinction coefficients of silicon nitride (SiN_x) and titanium-doped germanium dioxide (Ti:GeO_2), however, directly impacts the fundamental absorption limits [20] of their DSD designs. This is clearly observed in simpler binary systems, where the minimum achievable absorption for $\text{SiO}_2/\text{Ti:GeO}_2$ designs is fundamentally lower than for $\text{SiO}_2/\text{SiN}_x$ designs. To account for this difference, we have set different absorption targets: 0.5 ppm for the Ti:GeO_2 design and 1.5 ppm for the SiN_x design.

The optimized DSD coating designs are presented in Fig. 1, where layer thicknesses are plotted in optical units. The material refractive indices required to convert these to physical thicknesses are listed in Table I. The accompanying *supplementary material* [20] provides a comprehensive description of the optimization framework, the resulting designs' full optical characteristics, and a crucial baseline analysis. This baseline explains why these materials underperform in traditional binary stacks, thereby motivating the necessity of the DSD architecture developed here. Table II lists the predicted optical properties of the final designs. While the transmittance and absorption at 1064 nm adhere to the predefined design constraints, the transmittance at 532 nm is a resultant property of the *single-band* optimization. The reflection coefficient at the first interface is close to -1 , indicating a near-zero electric field at the surface, which minimizes sensitivity to surface contamination.

Experimental Validation and Results – To validate our design-to-fabrication pipeline, we realized the two ternary DSD coatings through a multi-step process, followed by a comprehensive and thorough campaign of characterization of their optical and mechanical performances.

The multi-material coating samples were grown at the Laboratoire des Matériaux Avancés [21] using a two-step deposition pro-

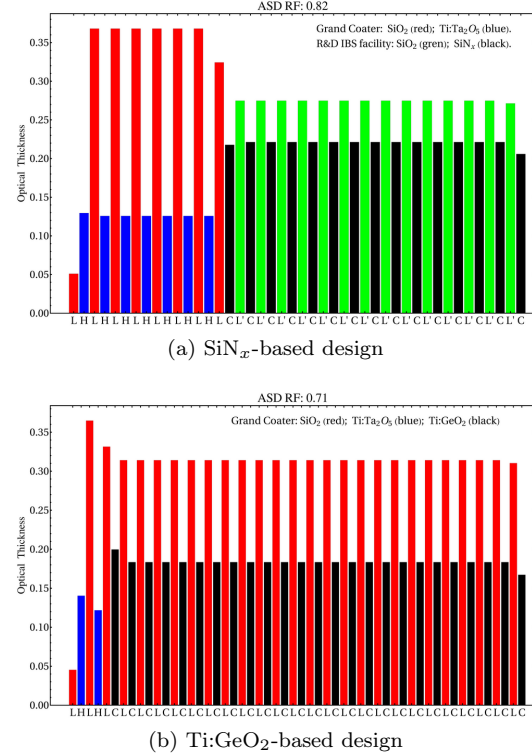


FIG. 1: Layout and predicted thermal noise performance (ASD RF) of the two optimized ternary mirror coatings realized in this work. Vacuum is on the left (the top) of the design, substrate is on the right of the figure. The bar colors correspond to the different dielectric materials. For the SiN_x -based design (a), the bottom stack consists of SiN_x (black) and SiO_2 (green) both deposited in an *R&D* IBS facility at LMA. The top stack consists of $\text{Ti:Ta}_2\text{O}_5$ (blue) and SiO_2 (red), both deposited in the main IBS facility at LMA (the Grand Coater). For the Ti:GeO_2 -based design (b), the bottom stack uses Ti:GeO_2 (black) and SiO_2 (red), while the top stack uses $\text{Ta}_2\text{O}_5\text{-TiO}_2$ (blue) and SiO_2 (red), all deposited in the LMA Grand Coater.

cess that, for the SiN_x case, required two different custom-developed ion-beam sputtering (IBS) systems. The lower $\text{SiN}_x/\text{SiO}_2$ stack was first grown in the so-called *R&D* system, af-

ter which the samples were transferred to the so-called *Grand Coater* for the deposition of the upper Ta_2O_5 - TiO_2 / SiO_2 stack. The use of two distinct systems was mandated by scheduling constraints on the Grand Coater, which is the primary machine for manufacturing mirror coatings for current gravitational-wave interferometers [18]. In both systems, samples were grown using accelerated Ar ions (~ 1 keV, ~ 1 Å) as sputtering particles. The working pressure during deposition was maintained at $\sim 10^{-4}$ mbar, with O_2 fed into the chamber for oxide layers [18, 26].

Transmittance spectra were acquired over the 400–1400 nm range using a PerkinElmer Lambda 1050 spectrophotometer. Optical absorption at 1064 nm was measured with a precision of < 0.5 ppm using a custom setup based on photo-thermal deflection [29]. The critical Brownian thermal noise was measured in the 30 Hz to 3 kHz frequency band using a folded Fabry-Perot cavity [30, 31]. This technique employs co-resonating TEM_{02} and TEM_{20} orthogonal laser modes to precisely isolate the coating's noise spectrum. The optical and mechanical parameters (refractive index, absorption, and internal friction) of the individual materials used in the design algorithm were sourced from prior, dedicated characterizations of single-layer samples [17–19].

SiN_x-based Coating. The first design uses a bottom stack of high contrast SiN_x / SiO_2 and a top stack of low-absorption $Ti:Ta_2O_5$. The optimized structure is shown in Fig. 1a. A split-annealing process was required to prevent the onset of crystallization in Ta_2O_5 - TiO_2 . We separately annealed the lower SiN_x / SiO_2 stack at higher temperature (900 °C for 10 hours), before depositing the upper Ta_2O_5 - TiO_2 / SiO_2 stack and annealing the whole DSD design at a lower temperature (600 °C for 10 hours). The measured and theoretical transmittance spectra for the SiN_x -based design is displayed in Fig. 3a, the experimental spectrum shows remarkable agreement with the theoretical curve, accurately reproducing the central wavelength and width of the high-reflectivity band, as well as the pass-band ripples. The modest accuracy at

shorter wavelengths, such as 532 nm, was anticipated, since the theoretical spectrum was generated using constant refractive indices (fixed at their 1064 nm values), thereby not accounting for the effects of material dispersion.

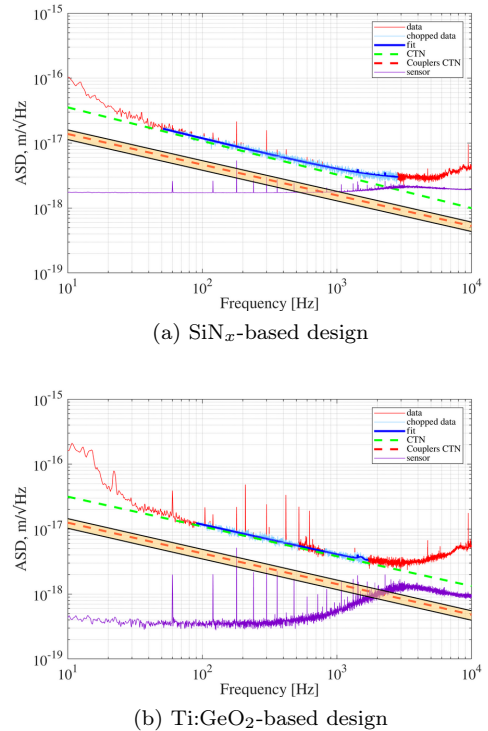


FIG. 2: CTN measurements of the two optimized ternary mirror coatings. (a) SiN_x -based design. (b) $Ti:GeO_2$ -based design. The experimental noise is presented as both a raw measurement (*data*) and a filtered trace (*chopped data*), from which noise around the harmonics of the 60 Hz power-line frequency has been removed. The solid curve, labeled *fit*, represents the estimated thermal noise.

Figure 2a presents the measured amplitude spectral density (ASD) for the optimized SiN_x -based design, obtained from noise measurements performed with the Coating Thermal Noise (CTN) interferometer. Again, the observed performance shows remarkable agreement with predictions (the measured proper-

ties in Table III closely match the design targets in Table II), exhibiting a thermal noise of $10.6 \times 10^{-18} \text{ m}/\sqrt{\text{Hz}}$. This corresponds to an ASD Reduction Factor (ASD RF) of 0.82 relative to the current LIGO and Virgo End Test Mass (ETM) coatings [26]. Furthermore, the measured spectral index of $\alpha = 0.5 \pm 0.03$ indicates a negligible dispersion of the mechanical parameters.

In addition, an absorption of approximately 1.5 ppm was measured.

Collectively, these results provide the crucial experimental validation of our entire methodology.

Ti:GeO₂-based Coating. To demonstrate the full potential of our validated framework, we applied it to a more advanced material system. We replaced the SiN_x/SiO₂ bottom stack with a Ti:GeO₂/SiO₂ one, a combination known for its potential for lower intrinsic losses [20]. The resulting optimized design is shown in Fig. 1b and its transmittance spectrum is shown in Fig. 3b showing a fair match between measurement and prediction.

The final absorption of 0.7 ppm (see Table III) was achieved through a dedicated multi-step procedure: first, the substrate underwent a 10-hour pre-annealing at 900°C. Subsequently, after the deposition of the first layer stack, a 100-hour anneal at 600 °C was performed. Finally, after the second deposition step, the entire coating was subjected to a final 100-hour annealing at 500°C.

As detailed in Table III, the resulting mirror exhibits good performance, with a measured thermal noise of $11.2 \pm 0.2 \times 10^{-18} \text{ m}/\sqrt{\text{Hz}}$, corresponding to an ASD RF of 0.81. The spectral index of $\alpha = 0.44$ confirms the presence of mechanical dispersion.

While the coating successfully achieved the goal of sub-ppm absorption (below its Carniglia limit [20]), the measured thermal noise performance (ASD RF of 0.81) did not fully meet the ambitious design target (ASD RF of 0.71 [20]). This deviation, mirrored by a measured transmittance of 8.8 ppm which exceeds the 5.6 ppm design constraint, along with the less perfect agreement in the transmittance spectrum

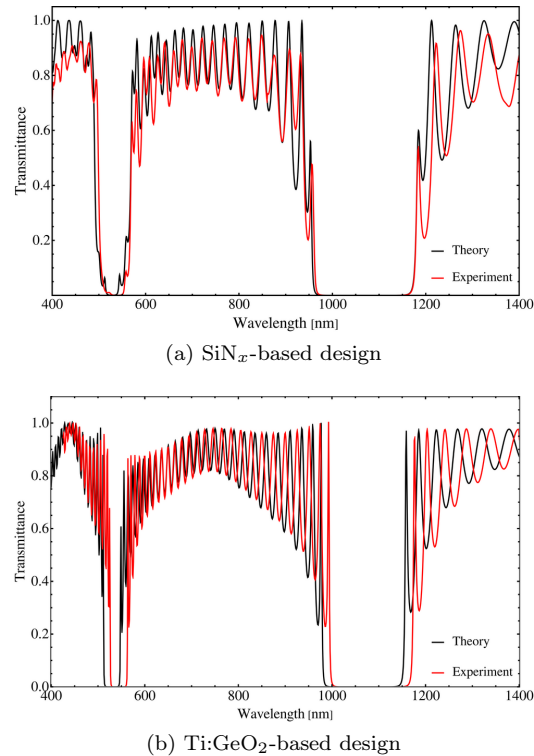


FIG. 3: Comparison of the measured (red curve) and theoretical (black curve) transmittance spectra for the two optimized ternary coatings: (a) the SiN_x-based design and (b) the Ti:GeO₂-based design. For both coatings, an excellent agreement is observed around the 1064 nm design wavelength, especially for the SiN_x based structure, validating the *quasi*-periodic design and the high precision of the fabrication process. The minor deviation at shorter wavelengths is expected, as the theoretical model does not account for material dispersion, assuming instead constant refractive indices based on their values at 1064 nm.

(Fig. 3b), suggests that realizing the full potential of this advanced material combination requires further study of the fabrication process, and its impact on the relevant material properties. To further investigate the source of this deviation, a dedicated tolerance analysis was

performed in [20]. The simulations show that the design is robust against independent

random layer thickness errors (± 0.5 nm for each layer) as well as against uncertainties in the material refractive indices (0.2%), with the ASD RF exhibiting a nearly Gaussian distribution with a standard deviation of less than 0.01%. Such a minimal variation from fabrication tolerances cannot account for the significant gap between the predicted and measured performance. This strongly suggests that the discrepancy is not due to simple stochastic errors but points to a more fundamental issue, such as an unforeseen material incompatibility or process-induced stress that is not captured by single-layer characterization. This confirms a crucial point: while the choice of materials sets the performance limit, mastering the complex interplay between materials during co-deposition and annealing is paramount to fully exploiting their potential.

Discussion and Outlook— This work presents the first successful experimental realization of multi-material optical coatings designed via multi-objective optimization, a milestone underscored by the flawless fabrication of two distinct prototypes. The good agreement between prediction and measurement for both distinct and complex ternary systems proves the robustness and predictive power of our design framework. This establishes a reliable methodology for creating bespoke optical coatings with tai-

lored properties that were previously inaccessible.

The realization of the SiN_x -based coating serves as a crucial proof-of-concept, since it demonstrates that even materials with relatively high absorption can be incorporated into a low-noise design. The subsequent realization of the Ti:GeO_2 -based coating, which leverages a more advanced but comparatively less-studied material, showcases the true potential of the validated method.

Acknowledgements— The CTN experiment is supported by the LIGO Laboratory. LIGO was constructed by the California Institute of Technology and Massachusetts Institute of Technology with funding from the National Science Foundation and operates under cooperative agreement PHY-1764464. CTN data analysis and figure generation were carried out using MATLAB software provided by The MathWorks, Inc.

The authors V.P., I.M.P., V.G. gratefully acknowledge support from the Istituto Nazionale di Fisica Nucleare (INFN) via the VIRGO and VIRGO-ET projects. We are also grateful to the members of the LIGO Optics Working Group and the Virgo Coating Research and Development for valuable discussions.

In the document repositories of the LIGO and Virgo Collaborations, this work has numbers LIGO-P2500607-v1 and VIR-0888A-25, respectively.

[1] See [OPTICA Milestone Events & Celebrations](#).

[2] H. J. Jawad and A. F. Sultan, *J. Opt.* **54**, 763–768 (2025). [doi:10.1007/s12596-024-01778-1](https://doi.org/10.1007/s12596-024-01778-1).

[3] C. Turnbaugh *et al.*, *Rev. Sci. Instrum.* **92**, 053005 (2021). [doi: 10.1063/5.0045496](https://doi.org/10.1063/5.0045496)

[4] J. Zhu, J. Zhu, X. Li *et al.*, *High Power Laser Sci. Eng.* **6**, e55 (2018). [doi:10.1017/hpl.2018.46](https://doi.org/10.1017/hpl.2018.46)

[5] J. Ye, E. Chin, and S. Lindquist, *Rev. Mod. Phys.* **84**, 1093 (2012).

[6] M. Aspelmeyer, T. J. Kippenberg, and Florian Marquardt, *Rev. Mod. Phys.* **86**, 1391 (2014).

[7] A. Ejlli *et al.*, *Phys. Rep.* **871**, 1 (2020). [doi:10.1016/j.physrep.2020.06.001](https://doi.org/10.1016/j.physrep.2020.06.001).

[8] M. Granata *et al.*, *Appl. Opt.* **59**, A229 (2020). [doi:10.1364/AO.377293](https://doi.org/10.1364/AO.377293)

[9] LIGO Scientific Collaboration, <https://ligo.caltech.edu/>; Virgo Collaboration, <https://www.virgo-gw.eu/>; KAGRA, <https://www.icrr.u-tokyo.ac.jp/en/facility/4219/>.

[10] R. Wang, Y. Li, and X. Qiao, *Lightwave Technol.* **41**, 4238 (2023). [doi: jlt-41-13-4238](https://doi.org/10.1109/LPT.2023.3660001)

[11] W. Yam, S. Gras, and M.

Evans, Phys. Rev. D **91**, 042002 (2015). [doi:10.1103/PhysRevD.91.042002](https://doi.org/10.1103/PhysRevD.91.042002).

[12] J. Steinlechner *et al.*, Phys. Rev. D **91**, 042001 (2015). [doi:10.1103/PhysRevD.91.042001](https://doi.org/10.1103/PhysRevD.91.042001).

[13] N. Demos, S. Gras, M. Evans, P. O'Brien, G. Billingsley, and L. Zhang, Class. Quantum Grav. **42**, 115012 (2025). [doi: 10.1088/1361-6382/add2c6](https://doi.org/10.1088/1361-6382/add2c6).

[14] V. Pierro *et al.*, Opt. Mater. **96**, 109269 (2019). [doi:10.1016/j.optmat.2019.109269](https://doi.org/10.1016/j.optmat.2019.109269).

[15] V. Granata, V. Pierro, and L. Troiano, Appl. Sci. **12**, 7680 (2022). [doi:10.3390/app12157680](https://doi.org/10.3390/app12157680).

[16] V. Pierro *et al.*, Phys. Rev. Research **3**, 023172 (2021). [doi:10.1103/PhysRevResearch.3.023172](https://doi.org/10.1103/PhysRevResearch.3.023172).

[17] K. Craig *et al.*, Phys. Rev. Lett. **122**, 231102 (2019). [doi:10.1103/PhysRevLett.122.231102](https://doi.org/10.1103/PhysRevLett.122.231102).

[18] S. C. Tait *et al.*, Phys. Rev. Lett. **125**, 011102 (2020). [doi:10.1103/PhysRevLett.125.011102](https://doi.org/10.1103/PhysRevLett.125.011102).

[19] H. Pan *et al.*, Phys. Rev. D **98**, 102001 (2018). [doi:10.1103/PhysRevD.98.102001](https://doi.org/10.1103/PhysRevD.98.102001).

[20] See Supplemental Material appended to this letter.

[21] D. Hadka and P. Reed, Evol. Comput. **21**, 231 (2013). [doi:10.1162/EVCO_a_00075](https://doi.org/10.1162/EVCO_a_00075).

[22] F. Abelès, J. Phys. Radium **11**, 307 (1950). [doi:10.1051/jphysrad:01950001107030700](https://doi.org/10.1051/jphysrad:01950001107030700).

[23] V. B. Braginsky, M. L. Gorodetsky, and S. P. Vyatchanin, in *Optical Coatings and Thermal Noise in Precision Measurement* (Cambridge University Press, Cambridge, 2012). [doi:10.1017/CBO9780511762314](https://doi.org/10.1017/CBO9780511762314)

[24] H. B. Callen and R. F. Greene, Phys. Rev. **86**, 702 (1952). [doi:10.1103/PhysRev.86.702](https://doi.org/10.1103/PhysRev.86.702).

[25] M. Granata *et al.*, Classical Quantum Gravity **37**, 095004 (2020). [doi:10.1088/1361-6382/ab77e9](https://doi.org/10.1088/1361-6382/ab77e9).

[26] A. Amato, *et al.*, Phys. Rev. D **111**, 042003 (2025), [doi:10.1103/PhysRevD.111.042003](https://doi.org/10.1103/PhysRevD.111.042003).

[27] L. Silenzi *et al.* (in preparation).

[28] Laboratoire des Matériaux Avancés (L.M.A.)-CNRS/IN2P3 web site : <https://lma.in2p3.fr/>

[29] A. C. Boccara, D. Fournier, W. Jackson, and N. M. Amer, Opt. Lett. **5**, 377 (1980). [doi:10.1364/OL.5.000377](https://doi.org/10.1364/OL.5.000377).

[30] S. Gras and M. Evans, Phys. Rev. D **98**, 122001 (2018). [doi:10.1103/PhysRevD.98.122001](https://doi.org/10.1103/PhysRevD.98.122001).

[31] S. Gras, H. Yu, W. Yam, D. Martynov, and M. Evans, Phys. Rev. D **95**, 022001 (2017). [doi:10.1103/PhysRevD.95.022001](https://doi.org/10.1103/PhysRevD.95.022001).

[32] M. Granata, V. Pierro, and I. M. Pinto, Ternary coating optimization update: more on the silicon nitride option, LIGO technical note n. [LIGO-G2101842](https://doi.org/10.1103/PhysRevD.95.022001) (2021).

TABLE I: Real part (n) and extinction coefficient (k) of the complex refractive index for the coating materials used in this work, specified at the 1064 nm design wavelength. Values are sourced from prior characterizations: SiO_2 and $\text{Ti:Ta}_2\text{O}_5$ from [18], SiN_x from [26], and Ti:GeO_2 is consistent with data in [17].

Material	Deposition System	Real Part (n)	Extinction Coeff. (k)
SiN_x	R&D	2.05	1.5×10^{-5}
SiO_2	R&D	1.475	5×10^{-8}
SiO_2	Grand Coater	1.45	3×10^{-8}
$\text{Ti:Ta}_2\text{O}_5$	Grand Coater	2.09	5×10^{-8}
Ti:GeO_2	Grand Coater	1.89	1.9×10^{-7}

TABLE II: Optical properties computed via optimization for both SiN_x and Ti:GeO_2 based designs.

DSD design	Complex reflection coefficient at vacuum interface	Transmittance @ 1064 nm	Absorption @ 1064 nm	Transmittance @ 532 nm	ASD RF
SiN_x -based	$-0.99814 - i0.060886$	5.6 ppm	1.45 ppm	11.6 ppm	0.82
Ti:GeO_2 -based	$-0.998396 - i0.0565713$	5.6 ppm	0.5 ppm	55.25 ppm	0.71

TABLE III: Measured properties of the realized ternary mirror coatings compared to current technology.

System	Deposition	Absorption [ppm]	Transmittance [ppm]	$S_{CB}(f) = A \times (100 \text{ Hz}/f)^\alpha$	ASD RF
Current ETM	Standard	0.5 ± 0.2	6.0 ± 0.2	13.7 ± 0.3	0.45 ± 0.02
SiN_x -based DSD	Split	1.4 ± 0.1	5.7 ± 0.2	10.6 ± 0.2	0.50 ± 0.03
Ti:GeO_2 -based DSD	Split	0.7 ± 0.1	8.8 ± 0.2	11.2 ± 0.2	0.44 ± 0.03

Supplementary Material: Experimental Realization of Optimized Ternary Mirror Coatings

Abstract

This supplementary material details the multi-objective optimization framework used to design advanced low-noise ternary mirror coatings for next-generation gravitational wave detectors. The primary goal is the simultaneous minimization of coating thermal noise, optical transmittance, and absorbance. By employing the Borg Multi-Objective Evolutionary Algorithm heuristic, this research explores the Pareto front of optimal trade-offs, providing the theoretical foundation required for experimental implementation.

The investigation presents simulations for two promising material systems: silicon nitride/silica ($\text{SiN}_x/\text{SiO}_2$) and titania-doped germania/silica ($\text{Ti}:\text{GeO}_2/\text{SiO}_2$). All simulations are grounded in experimentally-derived optical and mechanical parameters from prior characterizations of single-layer materials. The analysis focuses on advanced ternary structures, specifically the Double Stack of Doublets design, to overcome the performance limitations of traditional binary stacks.

The results underscore the critical importance of process consistency. While a simulated hybrid coating, using two different deposition facilities, exhibited a fragmented solution space, assuming a single high-quality deposition process for both the SiN_x and $\text{Ti}:\text{GeO}_2$ -based systems produced smooth, well-defined Pareto fronts. This analysis identifies concrete, optimized Double Stack of Doublets structures for both material systems, establishing them as viable and compelling candidates for experimental realization. As a primary example of the achieved performance, the $\text{Ti}:\text{GeO}_2$ -based design is predicted to yield a thermal noise reduction quantified by an Amplitude Spectral Density Reduction Factor of 0.71, while meeting the stringent optical requirements of 5.6 ppm transmittance and 0.5 ppm absorbance.

A concluding tolerance analysis, performed via Monte Carlo simulations, confirms the robustness of the proposed designs against state-of-the-art manufacturing imprecisions. This work therefore provides the essential theoretical blueprint for the successful fabrication and testing of these ultra-low-noise mirrors.

I. METHODOLOGY: OPTIMIZATION FRAMEWORK AND PHYSICAL MODELS

In this section we first introduce the multi-objective optimization framework that forms the core of our design strategy, followed by a description of the established physical models used to evaluate the coating's performance characteristics. This foundation is essential for the systematic exploration and identification of novel coating designs that push beyond current performance boundaries.

A. Multi-Objective Optimization Framework

In the design of high-performance dielectric mirrors for gravitational wave (GW) detectors, the engineering goal is not to optimize a single performance metric, but rather to find an optimal balance

between two physically competing requirements. As detailed by Refs. [1, 2], the problem centers on optimizing the vector of layer thicknesses, $\mathbf{z} = (z_1, \dots, z_{N_L})$, to simultaneously minimize the mirror's thermal noise, its optical transmittance and absorbance at the laser operating frequency (*single-band optimization*).

This focus on a *single-band optimization* is a deliberate strategic choice. Our primary goal was to identify the absolute best design possible for the main operating wavelength (1064 nm) in terms of minimal thermal noise. Introducing an additional constraint at another wavelength would inevitably restrict the available solution space and degrade the ultimate performance achievable. For the same reason, since all objectives are calculated at this single wavelength, material dispersion was not included in the model. However, the code supports the inclusion of dispersion in the calculation of optical properties.

A classical approach to such a problem would be to formulate it as a constrained optimization. For instance, one could seek to minimize the coating's thermal noise function, $\Phi_c(\mathbf{z})$, while ensuring that the transmittance, $\tau_c(\mathbf{z})$, and absorbance $\alpha_c(\mathbf{z})$, remain below some pre-defined thresholds. This is mathematically expressed as:

$$\min_{\mathbf{z} \in \Omega} \Phi_c(\mathbf{z}) \quad \text{subject to} \quad \tau_c(\mathbf{z}) \leq \tau_0, \quad \alpha_c(\mathbf{z}) \leq \alpha_0. \quad (\text{S1})$$

Here Ω defines the search space of physically allowable layer thicknesses.

A more comprehensive and powerful framework, which is used in our study, treats the problem from a true multi-objective standpoint. For this purpose, we employ the state-of-the-art Borg Multi-Objective Evolutionary Algorithm (Borg MOEA) heuristic [3]. The choice of this specific algorithm is deliberate and offers several key advantages over traditional methods:

- **Avoidance of Subjective Weighting:** A significant benefit of the Borg MOEA is that it eliminates the need for a single weighted cost function to account for competing objectives, as done in Ref. [4]. Such weighting schemes necessarily introduce a subjective pre-selection of constraints and can lead to an incomplete exploration of the solution space (see [5]). Our approach circumvents this by treating all objectives as equally important during the optimization phase.
- **Robust Pareto Front Discovery:** The Borg MOEA is specifically designed to effectively discover the complete set of objectively optimal solutions, i.e. the Pareto surface. The algorithm's output is therefore the Pareto front itself—a property of the problem space, not a product of subjective preferences introduced via weights.
- **Convergence Diagnostics:** The qualitative features of the computed Pareto front, such as its smoothness and continuity, provide valuable heuristic information. A well-defined, continuous front is a strong indicator that the optimization process has effectively converged toward the true optimal trade-off surface, giving us additional confidence in the robustness and quality of the final selected design.

In this paradigm, the goal is to discover the entire set of all possible optimal trade-offs. The problem is thus formulated as the simultaneous minimization of an objective vector:

$$\min_{\mathbf{z} \in \Omega} [\Phi_c(\mathbf{z}), \tau_c(\mathbf{z}), \alpha_c(\mathbf{z})]. \quad (\text{S2})$$

Solving this problem yields not a single solution but a set of non-dominated points forming the Pareto front, where improving one objective (e.g., reducing thermal noise) necessarily results in the

degradation of another (e.g., increasing transmittance). This approach provides designers with a complete map of optimal trade-offs, enabling an informed decision based on the holistic requirements of the detector, rather than being limited by an arbitrarily chosen initial constraint. The papers [1, 2] demonstrate that formulations (S1) and (S2) are mathematically equivalent, as they converge to the same solution. However, while formulation (S1) follows a constrained optimization approach, formulation (S2) adopts a true multi-objective strategy, leading to substantially different efficiency and exploration properties. As shown in our previous publications, the multi-objective formulation is not only more efficient but also enables a more exhaustive mapping of the optimal trade-offs. Consequently, exploring the Pareto front generated by formulation (S2) with a specialized, state-of-the-art heuristic is essential for fully understanding the performance limits of the system.

To evaluate the objective functions $\tau_c(\mathbf{z})$ and $\alpha_c(\mathbf{z})$ for any given thickness vector \mathbf{z} , a well-established optical model is employed, commonly known as the *transfer matrix method* [6].

This model was implemented within our proprietary codebase to ensure a tight and efficient integration with the Borg MOEA optimization engine, a critical requirement for handling the vast number of evaluations inherent to the heuristic search. For this reason, we did not use external packages like [7, 8]. The mirror coating is modeled as a stack of N_L dielectric layers, where each layer m is characterized by its thickness z_m and its complex refractive index, $n^{(m)}$. The complex nature of the refractive index accounts for material absorption.

The thermal noise objective, Φ_c , is directly related to the coating's Brownian thermal noise (see next section). Specifically, it is defined as the *amplitude spectral density* of this noise, which is the square root of the power spectral density (S_{CB}), evaluated at a representative frequency for GW detectors, typically $f = 100$ Hz. For practical comparison and to create a dimensionless figure of merit, it is convenient to normalize this value by the noise produced by the mirror reference design currently in use. This ratio will be referred to as the Amplitude Spectral Density Reduction Factor. A value less than unity indicates a performance improvement over the reference design.

A relevant special case for these mirrors is the double stack of doublets (DSD) design. For this specific DSD case, the optimization variables are therefore: the number of doublets N_1 for the first stack, along with the thickness vectors \mathbf{z}_1 and \mathbf{z}_2 for its constituent layers (each of length N_1); and the number of doublets N_2 for the second stack, with its corresponding thickness vectors \mathbf{s}_1 and \mathbf{s}_2 (each of length N_2).

The selection of the final design for fabrication is a distinct, *a posteriori* step performed on the computed Pareto front. This is a deterministic, two-stage methodology designed to yield a unique, optimal solution:

1. First, we filter the entire front to isolate the subset of solutions that satisfies the hard operational constraints of the detector (e.g., $\tau_c(\mathbf{z}) \leq \tau_0$ and $\alpha_c(\mathbf{z}) \leq \alpha_0$).
2. Second, from this feasible subset, we select the single design corresponding to the point with the **absolute minimum Brownian thermal noise**.

This two-stage process—first exploring the entire space of optimal trade-offs and then selecting based on hard constraints—therefore ensures the identification of a single optimal design for fabrication, guided by physical constraints rather than arbitrary cost functions.

B. Modeling Coating Thermal Noise Objective Functions

A foundational approach for describing the coating Brownian noise (S_{CB}) is the *Braginsky model* [9, 10]. This framework, discussed in the main letter, provides a direct calculation of thermal noise based on the materials' mechanical properties and layer thicknesses.

For a comprehensive description, the *Fejer Effective Medium Theory* [11] offers a more advanced treatment of the subject. The key advantage of the Fejer theory is its ability to explicitly distinguish between two fundamental dissipation mechanisms: *bulk loss* (ϕ_{\perp}) and *shear loss* (ϕ_{\parallel}). Despite its greater complexity, this model also allows the final thermal noise to be expressed in a way that is dependent on a linear combination of layer thicknesses, making it compatible with similar optimization strategies.

A significant practical challenge in applying the Fejer model is the experimental difficulty of independently measuring the bulk and shear loss angles [12, 13]. To simplify its application, it is common to make the approximation that these two loss components are equal ($\phi_{\perp} \approx \phi_{\parallel}$). Under this assumption, the Fejer model reduces to the Braginsky model, effectively framing the latter as a specific case of the more general theory.

Alternative models for describing coating thermal noise have been proposed [10, 14], which are potentially more accurate. However, these more complex models often fail to significantly outperform simpler ones when fitting experimental data. This is largely because current experimental uncertainties mask the finer details of the phenomenon.

II. THEORETICAL FRAMEWORK FOR BINARY STACKS

The performance of a standard quarter-wavelength (QWL) binary stack is critically limited by optical absorption, especially for demanding applications like GW detectors. This fundamental constraint is quantified by the *Koppelman limit* (henceforth KL) [15], which establishes the minimum possible absorption for a given pair of materials in a QWL stack. An approximate analytical form for the KL is given by:

$$\alpha_{\infty} \approx \frac{2\pi}{\lambda_0} \frac{n_L \kappa_H + n_H \kappa_L}{n_H^2 - n_L^2}, \quad (\text{S3})$$

where n and κ are the refractive index and extinction coefficient for the high-index (H) and low-index (L) materials, respectively, at the operating wavelength of $\lambda_0 = 1064$ nm.

To overcome the KL, Carniglia proposed a *tapered* design, where the layer thicknesses are apodized to minimize the electric field intensity within the more absorptive material [16]. This methodology allows the coating's absorption to approach the *Carniglia limit* (henceforth CL), a lower bound set purely by the bulk properties of the constituent materials. However, for applications as sensitive as GW detectors, this reduction in absorption often comes at the cost of increased Coating Thermal Noise (CTN), a critical performance-limiting factor. To address this inherent trade-off, we utilize the Borg Multi-Objective Evolutionary Algorithm (Borg-MOEA) framework (see Section IA) for a multi-objective optimization of the mirror coatings, balancing these competing requirements.

All results presented in this work are computed using a proprietary code that implements, for optical simulations, the exact Abelés transfer matrix method [6]. The code's accuracy is benchmarked against analytical solutions, including the limit described in Eq. (S3), which is valid for low-contrast QWL stacks.

III. SIMULATION AND OPTIMIZATION OF ADVANCED COATINGS

In this section optical and mechanical parameters (refractive index, absorption, and internal friction) of the individual materials used in the design algorithm were sourced from prior, dedicated characterizations of single-layer samples [17–19].

The purpose of the following analysis is twofold. For the $\text{Ti}::\text{GeO}_2$ system, our goal is to define the optimal theoretical performance, providing a clear and ambitious target for experimental validation. For the SiN_x system, despite its higher intrinsic absorption, the objective is to explore whether advanced DSD optimization can nonetheless yield a competitive design, offering a valuable alternative pathway. This dual investigation provides the essential theoretical blueprints to guide and assess the subsequent experimental fabrication of both coating designs.

A. Baseline Performance of Binary Stacks

Our investigation is structured to first analyze the fundamental performance of these materials in traditional binary QWL stacks. This initial step allows us to evaluate their intrinsic absorption properties with respect to the KL and CL. Subsequently, we will explore more advanced architectures to identify design strategies that can mitigate the critical trade-off between optical absorption and CTN.

As a first case study, we analyze the $\text{SiN}_x/\text{SiO}_2$ binary system. Although SiN_x is known to have a significant extinction coefficient [20], its analysis is fundamental for our work. It serves as a critical benchmark for the predictive methodology. By establishing theoretical performance limits—a KL of 44.9 ppm for a QWL stack (Fig. S1) and a CL of 9.607 ppm for a tapered design (Figs. S2-S3)—we create clear quantitative targets. Figure S4 displays a parametric analysis of these limits as a function of extinction coefficient material properties, providing further details for a quantitative understanding of the model.

The same framework is then applied to the $\text{Ti}::\text{GeO}_2/\text{SiO}_2$ system, a more recent material combination with lower intrinsic losses. For this stack, the calculated KL is 0.94 ppm (Fig. S5), which can be reduced to a CL of 0.76 ppm through design tapering (see analysis in Figs. S6-S7). The parametric analysis shown in Fig. S8 reveals a crucial design principle: the potential for improvement via tapering, quantified by the gap between the KL and CL, is directly governed by the contrast in complex refractive index coefficients between the high- and low-index materials. For the $\text{Ti}::\text{GeO}_2/\text{SiO}_2$ system, this contrast is significantly smaller than for the $\text{SiN}_x/\text{SiO}_2$ stack, which explains why the gap between its KL and CL is much less pronounced.

In conclusion, this analysis reveals a fundamental performance ceiling for these binary stacks. While design optimization via tapering proves effective (however, increasing mechanical losses), even the high-performance $\text{Ti}::\text{GeO}_2/\text{SiO}_2$ system struggles to achieve the sub-1-ppm absorption levels required for next-generation GW detectors. This limitation motivates the subsequent investigation of advanced ternary architectures. The goal will be to explore designs capable of further suppressing optical absorption without simultaneously increasing the equally critical CTN, thus breaking the performance trade-off inherent in simpler designs.

B. Design of Ternary DSD Architectures

To overcome the performance limits of binary stacks, we now investigate advanced ternary designs using a multi-objective optimization approach, in particular we use the DSD configuration. A top stack of low-loss $\text{Ti}::\text{Ta}_2\text{O}_5/\text{SiO}_2$ was used in all cases to minimize absorption, while the bottom stack was chosen to be either SiN_x -based or $\text{Ti}::\text{GeO}_2$ -based. We employ the Borg MOEA algorithm to navigate the complex trade-off space between three competing objectives: minimizing optical absorption (α_c), minimizing CTN (i.e. reduce ASD RF), and meeting the target transmittance (τ_c).

This analysis focuses on the optimization landscape itself, comparing three distinct cases: an ideal silicon nitride (SiN_x)-based coating, assuming all deposition is performed by a Grand Coater (GC); a practical hybrid SiN_x coating obtained in a two-step deposition process involving the *R&D* deposition system followed by GC; and a titanium-doped germanium oxide ($\text{Ti}::\text{GeO}_2$)-based coating, also assuming all-GC deposition.

1. Ideal SiN_x Design (All-GC)

First, we consider an idealized SiN_x -based design, assuming all layers can be deposited in the high-quality GC facility. The resulting three-dimensional Pareto front, shown in Fig. S9, is smooth and continuous. This indicates a well-behaved optimization problem, where a clear and unbroken set of optimal trade-off solutions exists. The two-dimensional projections (Fig. S10) allow for a clearer visualization of the direct trade-offs between pairs of objectives, from which a final design can be selected. Figure S11 shows the layer structure of one such optimal solution, uniquely determined by the constraints $\tau_c \leq 5.6$ ppm and $\alpha_c \leq 1.5$ ppm. This result demonstrates a successful outcome of the optimization process for this ideal case.

2. Hybrid SiN_x Design

We then analyze a more practical scenario where the coating is produced via a hybrid sputtering process. In this method, an initial SiN_x -based stack is deposited on the substrate using the *R&D* system, after which a second stack of Silica/Titania-doped Tantala is deposited on top via GC sputtering. This case contrasts sharply with the ideal one. The resulting Pareto front (Fig. S12) is fragmented and discontinuous. This is a critical finding: the use of higher-loss *R&D* system-deposited silica in the bottom part of the stack changes the structure of the solutions space. This distinct behavior of the *R&D* system-silica renders the system *effectively quaternary*, a condition for which the standard ternary DSD optimization strategy is ill-suited.

This fragmentation severely constrains the available solution space, creating *forbidden* regions of performance, particularly visible in the projection between absorbance and thermal noise (Fig. S13). The scattered nature of the optimal solutions highlights the performance degradation and the difficulty in finding a robust design. Figure 1a of the main letter shows the DSD structure of the minimal noise design selected from the Pareto front, which satisfies the constraints $\tau_c \leq 5.6$ ppm and $\alpha_c \leq 1.5$ ppm. However, due to the aforementioned fragmentation and discontinuity of the Pareto front, this design achieves an absorbance value of $\alpha_c = 1.44$ ppm.

3. $\text{Ti}::\text{GeO}_2$ Design (All-GC)

Finally, we apply the optimization framework to the $\text{Ti}::\text{GeO}_2$ -based system, where all layers are deposited using the consistent, high-quality GC process. As shown in Fig. S15, the resulting Pareto front is once again smooth and continuous, analogous to the ideal SiN_x case. This reinforces the conclusion that process consistency and high-quality materials are key to a well-behaved optimization landscape. The 2D projections in Fig. S16 illustrate the clear trade-offs, and Fig. 1b, displayed in the letter, presents the optimal layer recipe selected from this well-defined front.

In conclusion, from the set of Pareto-optimal solutions, we selected the design that minimizes the ASD RF while satisfying the optical constraints ($\tau_c \leq 5.6$ ppm and $\alpha_c \leq 1.5$ ppm for SiN_x ,

$\alpha_c \leq 0.5$ ppm for Ti::GeO₂). These designs, for the three cases, are shown in Fig. S11, and in Fig. 1a and b of the letter.

C. Comparative Performance and Manufacturing Tolerance

A comparative analysis of the optical properties reinforces the above conclusions. The transmittance spectra for all optimal designs meet the high-reflectivity requirement at $\lambda_0 = 1064$ nm as displayed in Figs. 3a and b of the letter. However, the layer-by-layer absorption profiles reveal the core limitation. For the SiN_x design, the SiN_x layers are the dominant source of absorption, with contributions orders of magnitude higher than any other material (Fig. S14). This makes it fundamentally challenging to reach sub-ppm levels. In contrast, although the Ti::GeO₂ layers are also the primary absorbers in their stack, their intrinsic optical loss is low enough that the overall coating absorption remains at the 0.5 ppm target (Fig. S17). This highlights the success of the DSD architecture in managing absorption (i.e. it is possible to *circumvent* the CL) by placing the lossier materials deeper in the stack, where the electric field is weaker.

To ensure the practical viability of the optimized coating designs, a tolerance analysis was performed to assess their robustness against manufacturing errors. We performed a Monte Carlo simulation (10^5 trials) that incorporates random perturbations on both the layer thicknesses and the refractive indices of the materials. The methodology and parameters for this expanded analysis are detailed below:

- **Perturbed Parameters:** The simulation introduces random, independent uncertainties to two key parameters. Firstly, the physical thickness of each layer, as this is the quantity directly controlled and subject to error during the deposition process. Secondly, the refractive index for each material.
- **Uncertainty Magnitudes:** The independent thickness uncertainty of ± 0.5 nm (modeled as a uniform distribution) is representative of the state-of-the-art precision achievable with the GC [21], that is the advanced ion-beam sputtering systems used for fabricating mirrors for gravitational-wave detectors. The uncertainty for the refractive indices was modeled based on typical run-to-run variations observed in our deposition systems, corresponding to a relative uncertainty of 0.2%.

The resulting statistical distributions for the key performance metrics of absorbance and transmittance are shown in the Figs. S18, and S19. The analysis reveals that the designs are highly robust. The narrow probability distributions for both absorbance (a) and transmittance (b) indicate that the optical properties are stable and not overly sensitive to typical random errors in layer thickness and refractive index. Furthermore, when subjected to the same random thickness errors, the resulting ASD RF values form a distribution that is approximately Gaussian. This distribution is exceptionally narrow, with a standard deviation on the order of 0.01% relative to the mean value for both the proposed design.

A summary of the final performance metrics is presented in Table S1. The results show that Ti::GeO₂-based DSD design achieves the lowest thermal noise (ASD RF = 0.71) while simultaneously meeting the aggressive sub-0.5 ppm absorbance target.

TABLE S1: Summary of predicted performance. This table compares the fundamental absorption limits of the binary material pairs (KL, and CL) with the final achieved metrics of the optimized ternary DSD designs. The results highlight how the DSD architecture allows the final coating to achieve performance levels beyond the binary limits. All values are theoretical predictions intended as experimental targets.

Design Case	Binary KL [ppm]	Binary CL [ppm]	ASD RF	Transmittance τ_c [ppm]	Absorbance α_c [ppm]
Ideal SiN _x (all GC)	44.9	9.61	0.73	5.6	1.50
Hybrid SiN _x (R&D deposition - GC)	46.8	14.4	0.82	5.6	1.44
Ti::GeO ₂ (all GC)	0.94	0.76	0.71	5.6	0.50

[1] V. Granata, V. Pierro, and L. Troiano, *Appl. Sci.* **12**, 7680 (2022). [doi:10.3390/app12157680](https://doi.org/10.3390/app12157680).

[2] V. Pierro *et al.*, *Opt. Mater.* **96**, 109269 (2019). [doi:10.1016/j.optmat.2019.109269](https://doi.org/10.1016/j.optmat.2019.109269).

[3] D. Hadka and P. M. Reed, *Evol. Comput.* **21**, 231 (2013). [doi: 10.1162/EVCO_a_00075](https://doi.org/10.1162/EVCO_a_00075)

[4] G. Venugopalan, F. Salces-Cárdenas, K. Arai, and R. X. Adhikari, *Opt. Express* **32**, 11751 (2024). [doi:10.1364/OE.513807](https://doi.org/10.1364/OE.513807)

[5] R. T. Marler and J. S. Arora, *Struct. Multidiscip. Optim.* **26**, 369–395 (2004). [doi:10.1007/s00158-003-0368-6](https://doi.org/10.1007/s00158-003-0368-6)

[6] F. Abelès, *J. Phys. Radium* **11**, 307 (1950). [doi:10.1051/jphysrad:01950001107030700](https://doi.org/10.1051/jphysrad:01950001107030700).

[7] R. C. Rumpf, *Progress In Electromagnetics Research* **35**, 241 (2011). [doi:10.2528/PIERB11083107](https://doi.org/10.2528/PIERB11083107)

[8] A. Luce, A. Mahdavi, F. Marquardt, and H. Wankerl, *J. Opt. Soc. Am. A* **39**, 1007 (2022). [doi:10.1364/JOSAA.450928](https://doi.org/10.1364/JOSAA.450928)

[9] V. B. Braginsky, M. L. Gorodetsky, and S. P. Vyatchanin, *Phys. Lett. A* **264**, 1 (1999). [10.1016/S0375-9601\(99\)00785-9](https://doi.org/10.1016/S0375-9601(99)00785-9)

[10] A. Gurkovsky and S. Vyatchanin, *Phys. Lett. A* **374**, 3267 (2010). [doi:10.1016/j.physleta.2010.06.012](https://doi.org/10.1016/j.physleta.2010.06.012)

[11] M. M. Fejer, *Effective Medium Description of Multilayer Coatings*, LIGO Technical Document No. T2100186 (2021). <https://dcc.ligo.org/LIGO-T2100186>

[12] G. Vajente, M. Fazio, L. Yang, A. Gupta, A. Ananyeva, G. Billingsley, and C. S. Menoni, *Phys. Rev. D* **101**, 042004 (2020). [doi:10.1103/PhysRevD.101.042004](https://doi.org/10.1103/PhysRevD.101.042004)

[13] M. R. Abernathy, S. L. Gras, A. G. Tuyen, J. Cripe, K. L. Dooley, K. A. Haughian, G. M. Harry, and M. Evans, *Phys. Lett. A* **382**, 2282 (2018). [doi: 10.1016/j.physleta.2017.08.007](https://doi.org/10.1016/j.physleta.2017.08.007)

[14] T. Hong, H. Yang, E. K. Gustafson, R. X. Adhikari, and Y. Chen, *Phys. Rev. D* **87**, 082001 (2013). [doi:10.1103/PhysRevD.87.082001](https://doi.org/10.1103/PhysRevD.87.082001)

[15] G. Koppelman, *Ann. Phys. (Leipzig)* **460**, 388 (1960). [doi:10.1002/andp.19604600704](https://doi.org/10.1002/andp.19604600704)

[16] C. K. Carniglia and J. H. Apfel, *J. Opt. Soc. Am.* **70**, 523 (1980). [doi:0.1364/JOSA.70.000523](https://doi.org/10.1364/JOSA.70.000523)

[17] M. Granata *et al.*, *Appl. Opt.* **59**, A229 (2020). [doi:10.1364/AO.377293](https://doi.org/10.1364/AO.377293)

[18] M. Granata *et al.*, *Classical Quantum Gravity* **37**, 095004 (2020). [doi:10.1088/1361-6382/ab77e9](https://doi.org/10.1088/1361-6382/ab77e9).

[19] M. Granata, V. Pierro, and I. M. Pinto, Ternary coating optimization update: more on the silicon nitride option, LIGO technical note n. [LIGO-G2101842](https://dcc.ligo.org/LIGO-G2101842) (2021).

[20] A. Amato, *et al.*, *Phys. Rev. D* **111**, 042003 (2025), [doi:10.1103/PhysRevD.111.042003](https://doi.org/10.1103/PhysRevD.111.042003).

[21] LMA technical staff, private communication.

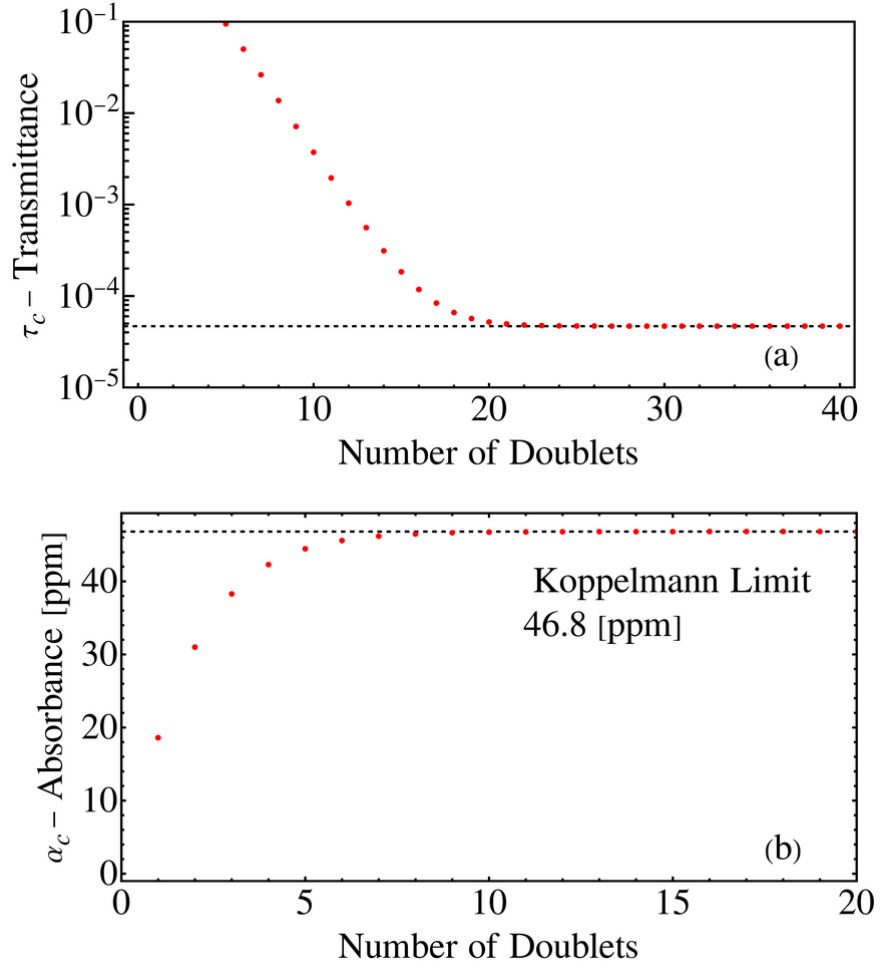


FIG. S1: (a) Transmittance (τ_c) and (b) absorbance (α_c) for a QWL multilayer stack of Silica/SiN_x as a function of the number of doublets. The transmittance is shown on a logarithmic scale and decreases as more layers are added. The absorbance, measured in parts per million (ppm), increases. Both saturate at the Koppelmann Limit. The limit is 44.9 ppm for a stack using all GC silica, and 46.8 ppm (as shown in this plot) when using silica of the *R&D* deposition system for the bottom layers, corresponding to the hybrid design. Here the extinction coefficient is $\kappa_{SiN_x} = 1.5 \times 10^{-5}$.

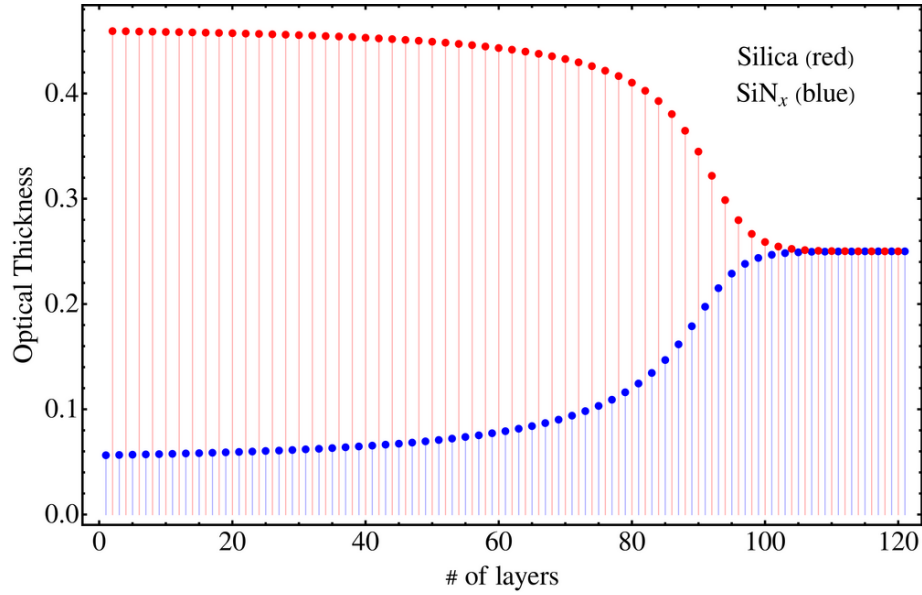


FIG. S2: Schematic representation of the tapered layer thicknesses in the $\text{SiN}_x/\text{SiO}_2$ stack designed according to the Carniglia method. The high-index SiN_x layers (blue) are progressively thinned towards the front of the mirror (left), while the low-index SiO_2 layers (red) are thickened to minimize absorption.

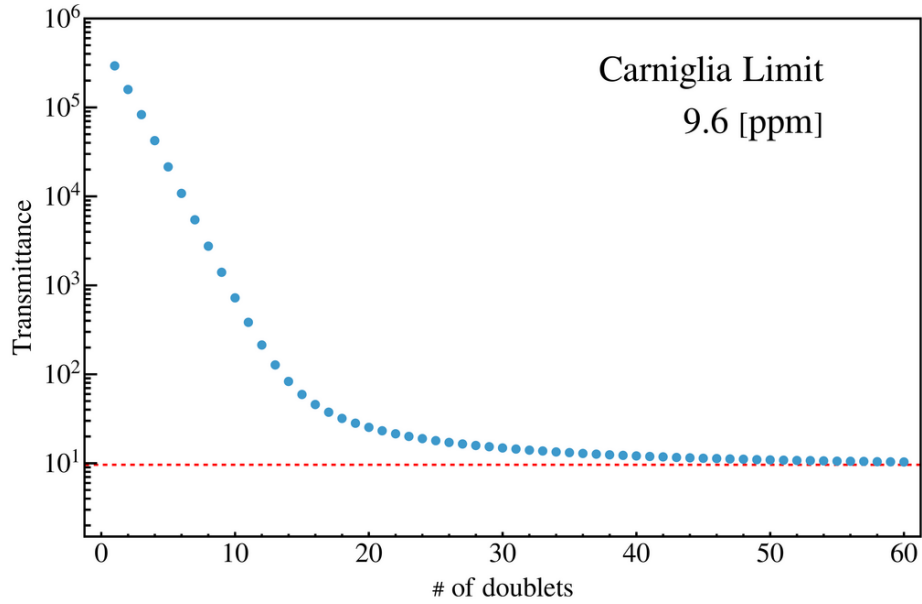


FIG. S3: Transmittance as a function of the number of layer pairs for the tapered $\text{SiN}_x/\text{SiO}_2$ stack. The transmittance asymptotically approaches the Carniglia Limit of 9.607 ppm, demonstrating a significant reduction in absorption compared to the standard quarter-wave stack shown in Fig. S1.

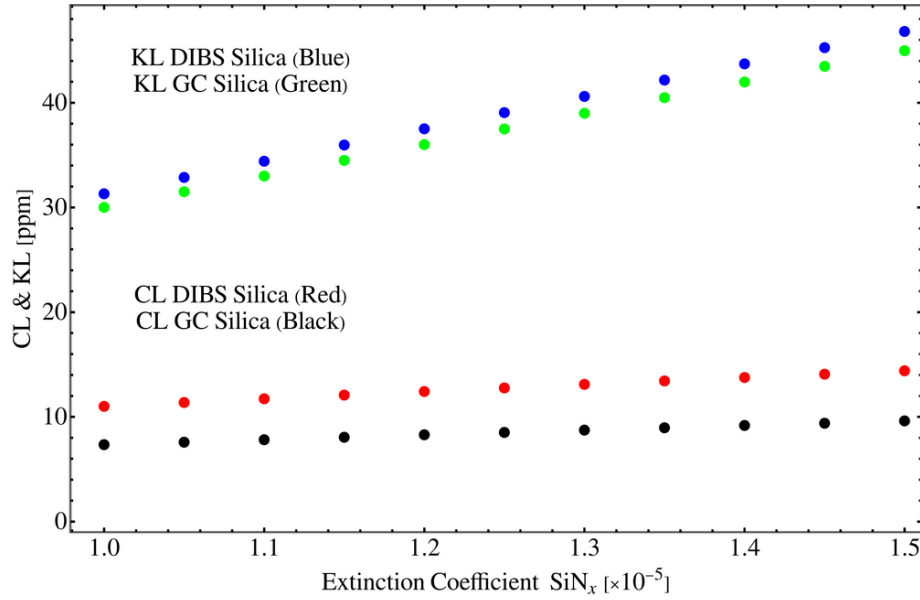


FIG. S4: Comparison of the KL and CL for SiN_x/SiO_2 stacks as a function of the SiN_x extinction coefficient (κ_{SiN_x}). Results are shown for both GC and *R&D* deposition system silica. The CL is consistently lower than the KL, and the difference becomes more significant as the material absorption increases.

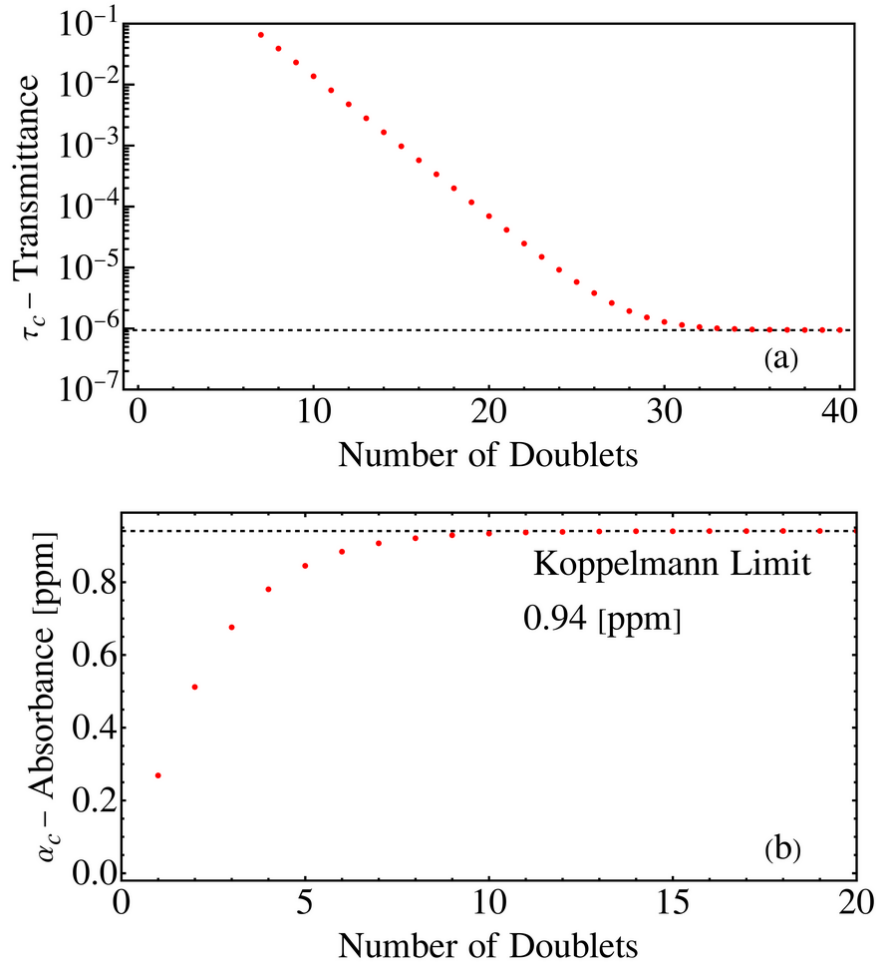


FIG. S5: (a) Transmittance (τ_c) and (b) absorbance (α_c) for a QWL multilayer stack of Silica/Ti::GeO₂ as a function of the number of doublets. The transmittance is shown on a logarithmic scale, and the absorbance is measured in ppm. Both saturate at the Koppelmann Limit of 0.94 ppm.

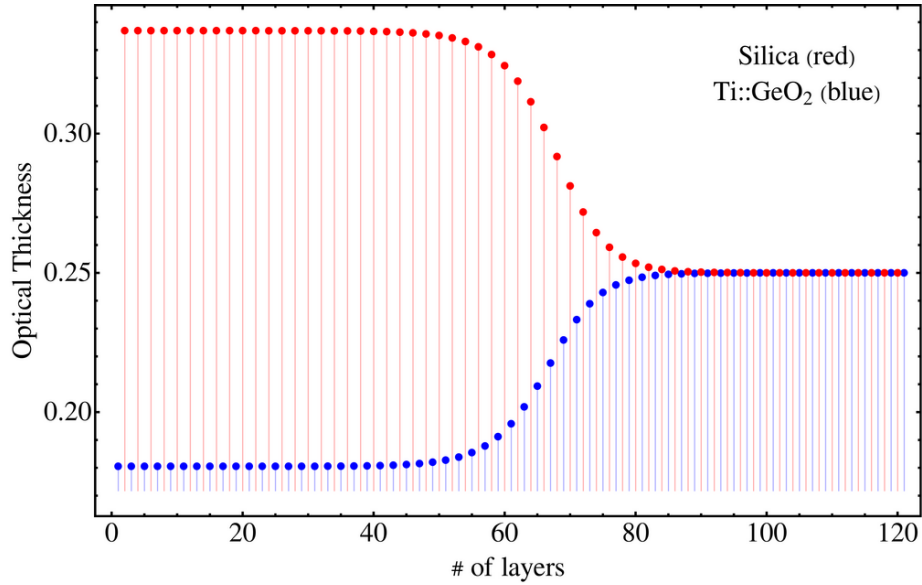


FIG. S6: Schematic of the tapered layer design for the $\text{Ti}:\text{GeO}_2/\text{SiO}_2$ stack, following the Carniglia optimization method to minimize absorption.

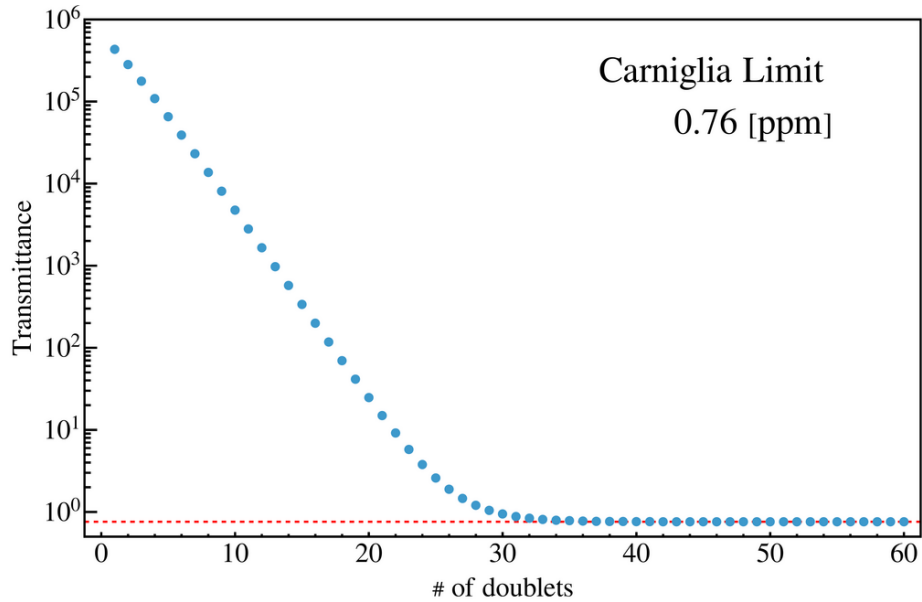


FIG. S7: Transmittance approaching the Carniglia Limit for the optimized $\text{Ti}:\text{GeO}_2/\text{SiO}_2$ stack. The asymptotic value represents the lowest possible absorption achievable with this material pair and design methodology (i.e. 0.76 ppm).

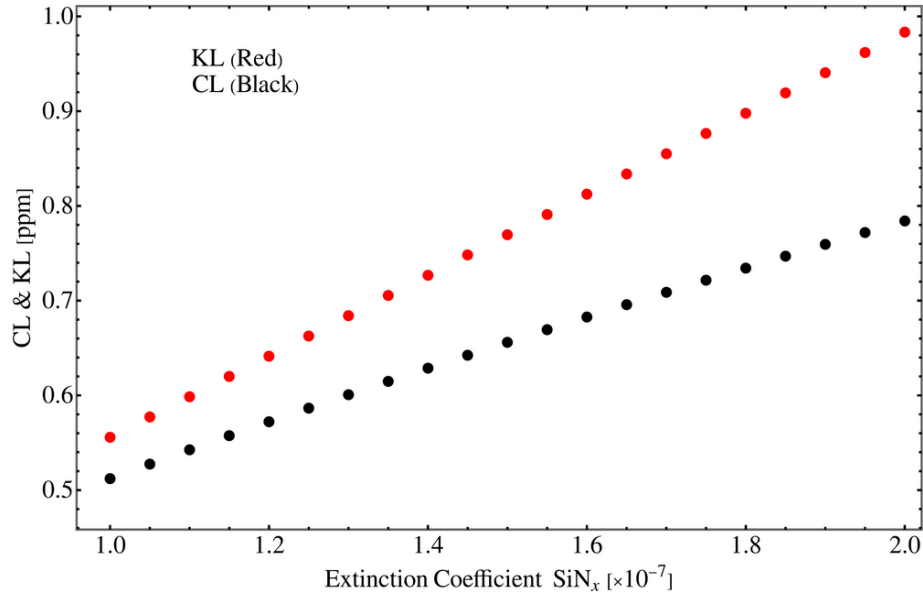


FIG. S8: Comparison of KL and CL for the $\text{Ti}::\text{GeO}_2/\text{SiO}_2$ system. The plot illustrates the theoretical minimum absorption for both standard (KL) and optimized (CL) designs. The gap between KL and CL is smaller than for the SiN_x case due to the lower extinction coefficient contrast.

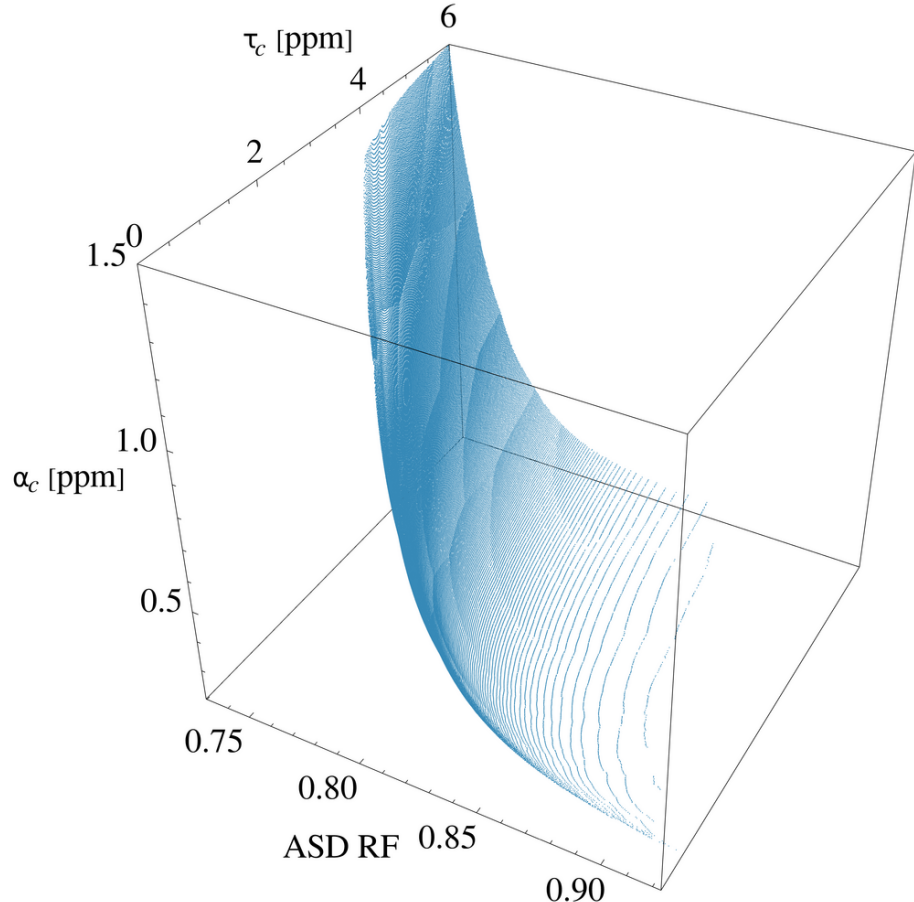


FIG. S9: Three-dimensional Pareto front for the SiN_x DSD coating obtained from multi-objective optimization using Borg MOEA algorithm, showing the trade-offs between optical absorption (α_c), transmittance (τ_c), and ASD RF for coating design. The surface represents non-dominated solutions optimizing noise reduction performance relative to the reference coating.

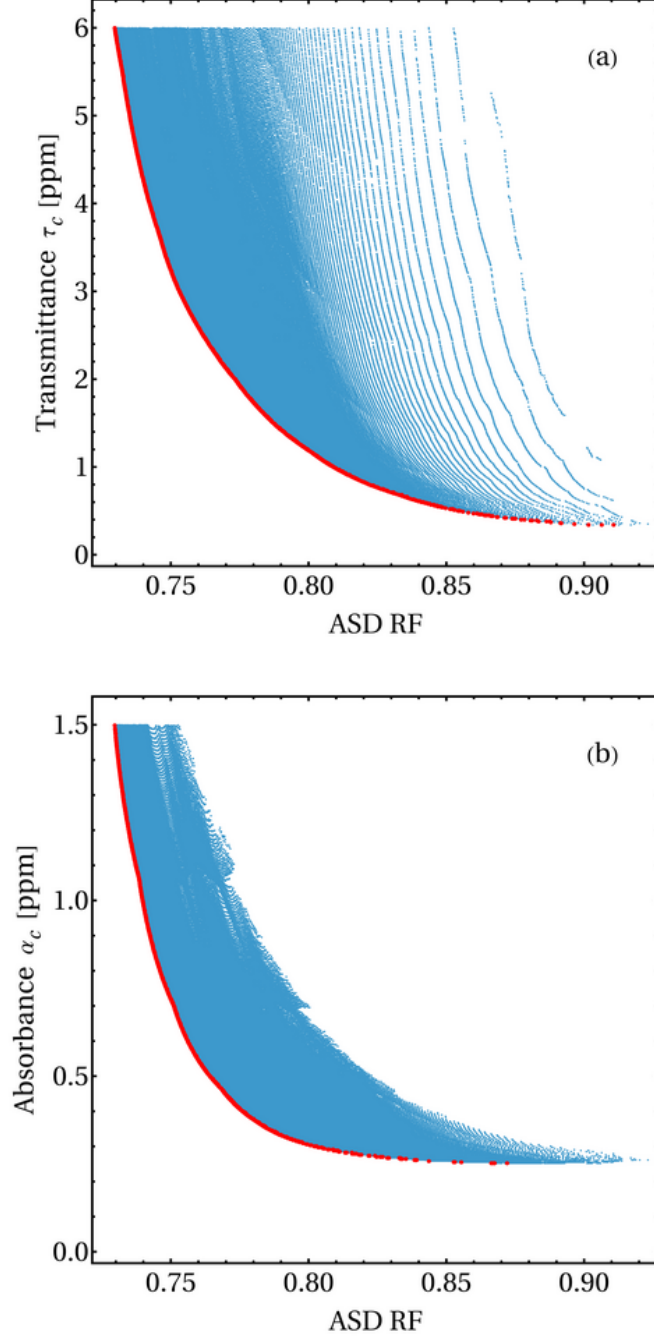


FIG. S10: Two-dimensional projections of the Pareto front for the SiN_x -based DSD design, illustrating the trade-offs between key performance metrics. (a) Transmittance (τ_c) versus ASD RF. (b) Absorbance (α_c) versus ASD RF. The red line in each plot marks the boundary of optimal solutions, representing the best achievable performance for each pair of objectives. This solution space is used to select the final coating design based on performance constraints.

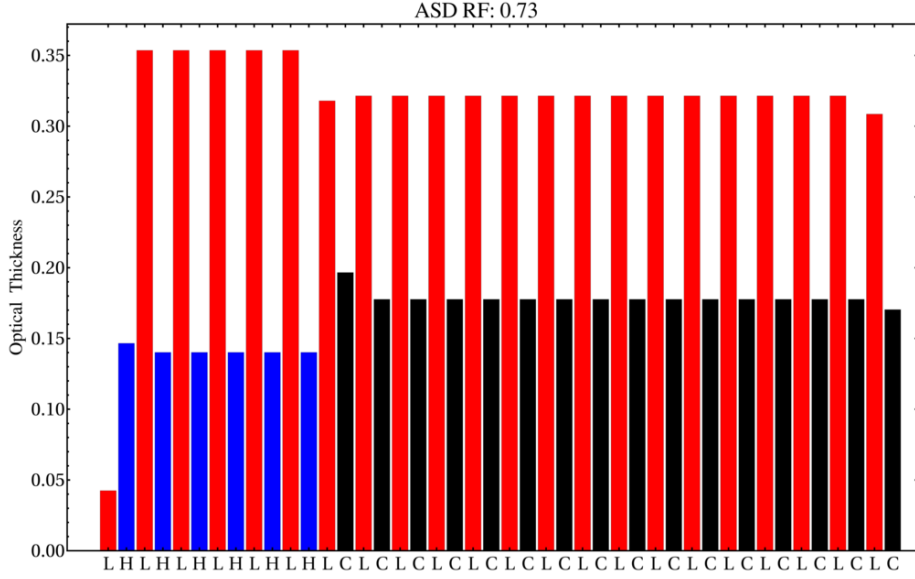


FIG. S11: The optimal layer structure selected from the Pareto front for the ideal SiN_x design. This design corresponds to the solution in the top-left region of the plots in Fig. S10, minimizing thermal noise while meeting the optical constraints. The bar chart details the optical thickness of each layer in the stack, the structure is $(\text{LH})^6(\text{LC})^{16}$ (here $N_1 = 6$ and $N_2 = 16$), where the labels L, H, and C denote silica, titania-doped tantalum, and SiN_x respectively.

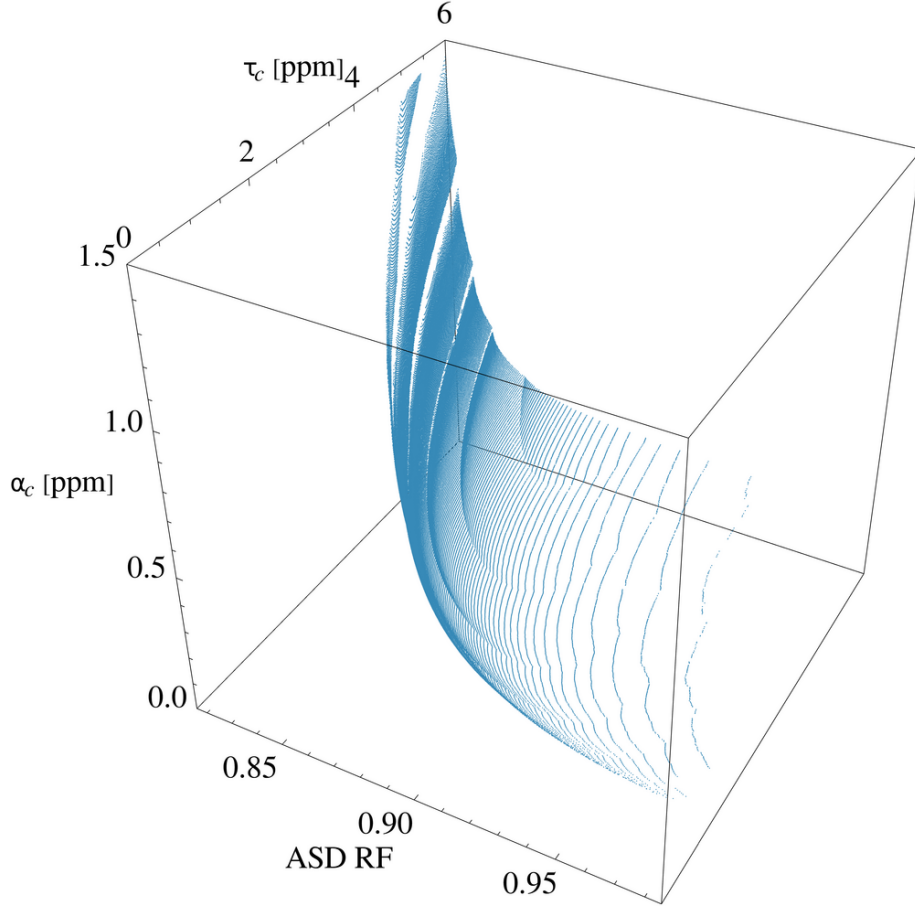


FIG. S12: Three-dimensional Pareto front for the hybrid SiN_x based DSD coating prepared by *R&D* system-GC. The discontinuity in the front highlights a constrained solution space and forbidden performance regions, which are attributed to the higher optical loss of the *R&D* deposition system silica. This distinct behavior of silica renders the system effectively quaternary, indicating that the DSD optimization strategy is ill-suited for this material combination.

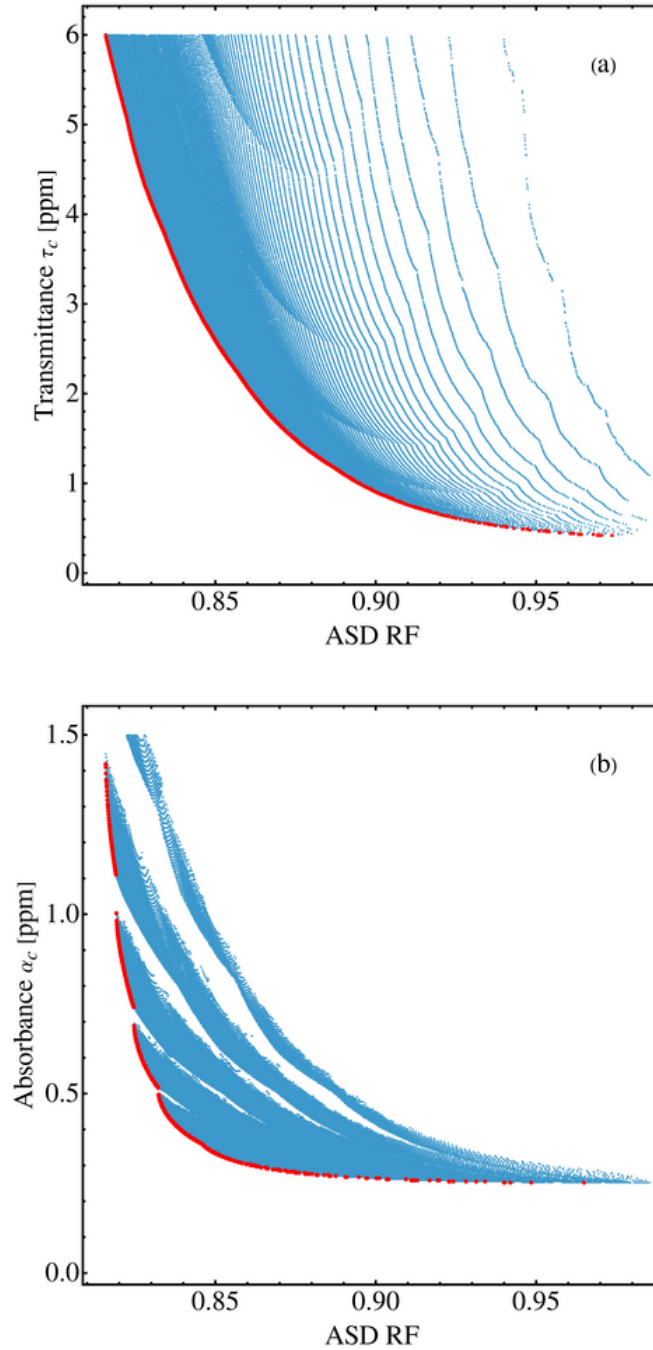


FIG. S13: Two-dimensional projections of the Pareto front for the hybrid SiN_x -based DSD design. The fragmentation and scattering of the optimal solutions, especially when compared to Fig. S10, highlight the performance degradation caused by the use of higher-loss *R&D* deposition system silica in the bottom stack.

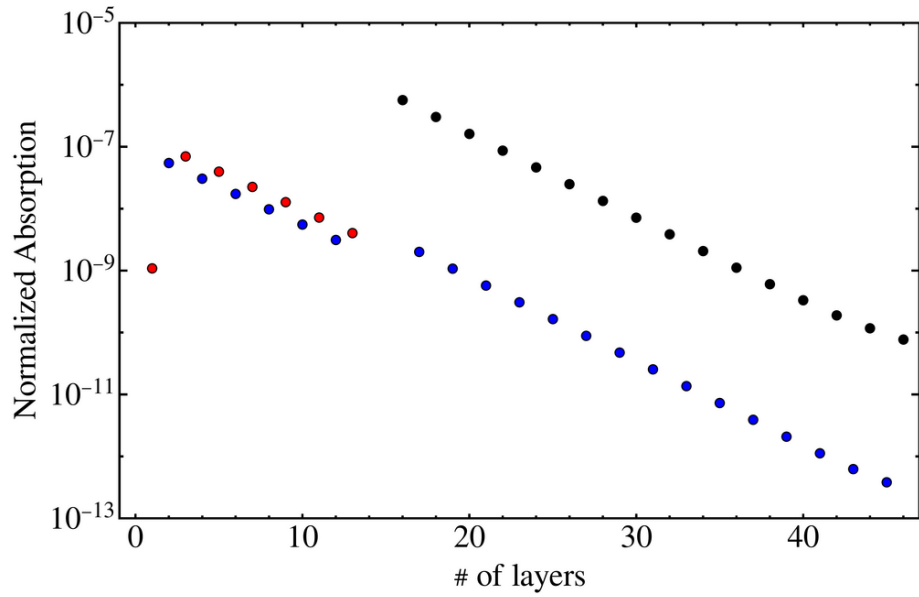


FIG. S14: Layer-by-layer contribution to the total absorption for the ideal SiN_x design. Total absorbance of the coating is 1.5 ppm. The colors identify the material for each layer: SiN_x (black), SiO_2 (red), named L, and $\text{Ti:Ta}_2\text{O}_5$ (blue). SiN_x is the dominant contributor.

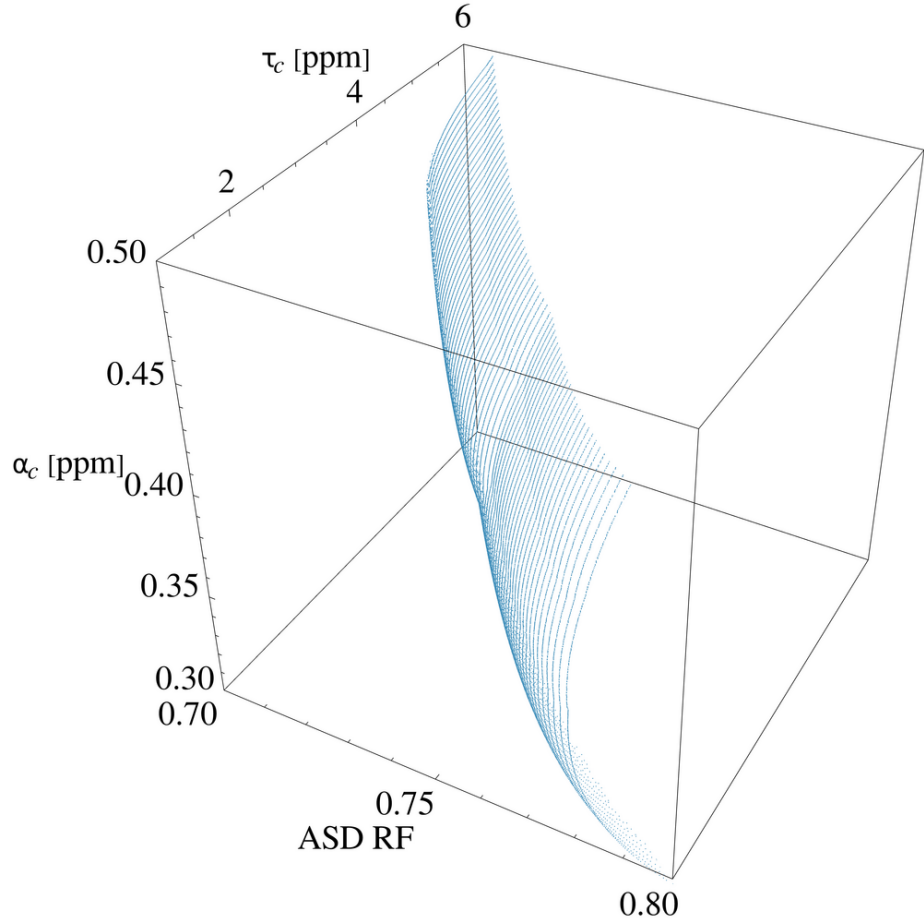


FIG. S15: Three-dimensional Pareto front for the Ti::GeO₂-based DSD coating. The smooth, continuous surface illustrates the well-defined trade-offs achievable with an all-GC deposition process.

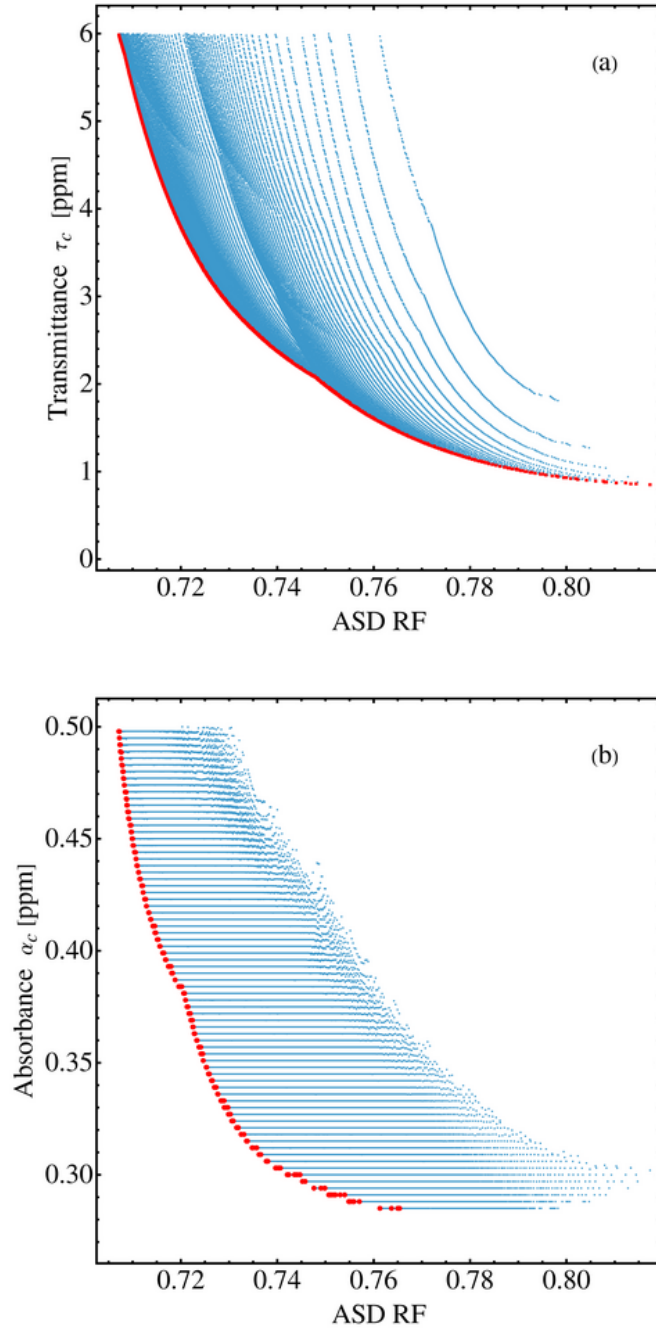


FIG. S16: Two-dimensional projections of the Pareto front for the Ti::GeO₂-based DSD design. (a) Transmittance (τ_c) versus ASD RF. (b) Absorbance (α_c) versus ASD RF. The solid red lines mark the boundary of optimal solutions.

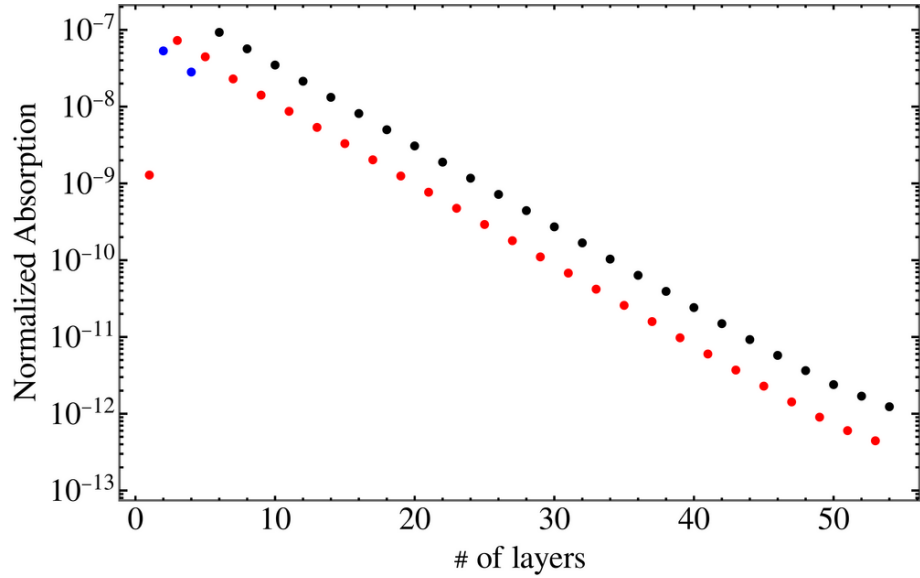


FIG. S17: Layer-by-layer contribution to total absorption for the optimized $\text{Ti}::\text{GeO}_2$ -based design. The total absorbance is 0.5 ppm. The colors identify the material for each layer: $\text{Ti}::\text{GeO}_2$ (black), SiO_2 (red), and $\text{Ti}::\text{Ta}_2\text{O}_5$ (blue). The $\text{Ti}::\text{GeO}_2$ layers are the main, but manageable, contributors to absorption.

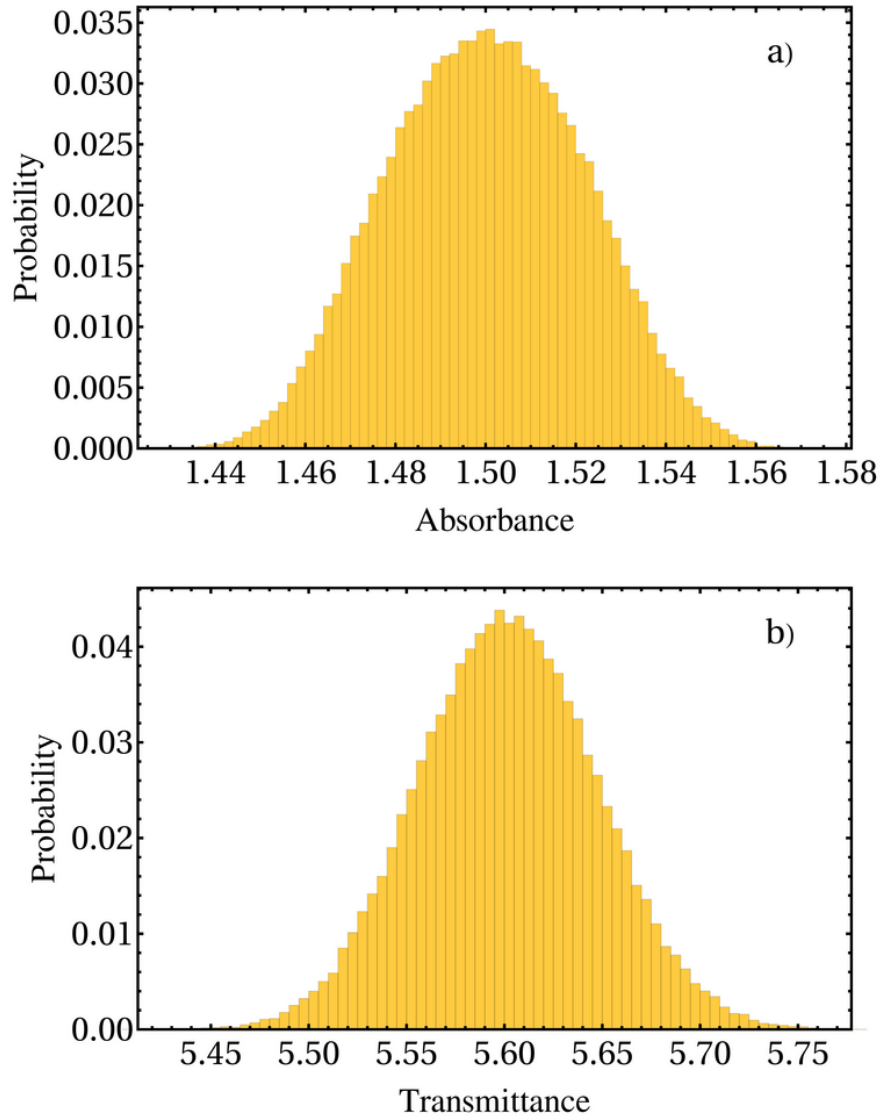


FIG. S18: Tolerance analysis for the optimized SiN_x -based design. The plots show the statistical distribution of (a) absorbance and (b) transmittance resulting from a Monte Carlo simulation (10^5 trials) where an independent random thickness uncertainty of ± 0.5 nm per layer and 0.2% uncertainty on refractive index. The results show values centered at 1.5 ppm for absorbance and 5.6 ppm for transmittance (that are the nominal values).

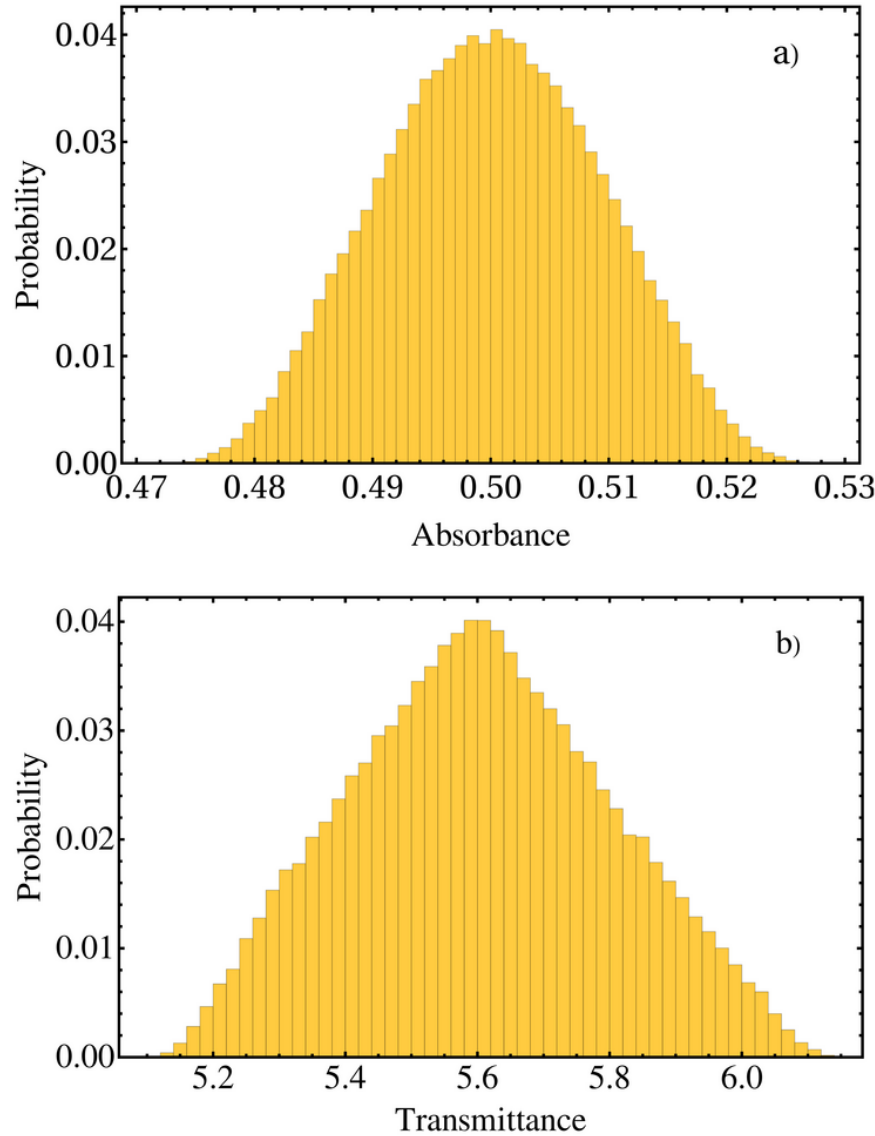


FIG. S19: Tolerance analysis for the optimized Ti:GeO₂-based design. The plots show the statistical distribution of (a) absorbance and (b) transmittance resulting from a Monte Carlo simulation (10^5 trials) where an independent random thickness error of ± 0.5 nm was applied to each layer and 0.2% uncertainty on refractive index. The narrow distributions are centered at the target values of 0.5 ppm for absorbance and 5.6 ppm for transmittance (that are the nominal values).